Predictive value of spectral dual-detector computed tomography for *PD-L1* expression in stage I lung adenocarcinoma: development and validation of a novel nomogram

Tong Wang[1], Zheng Fan[2], Yong Yue[1], Xiaomei Lu[3], Xiaoxu Deng[4], Yang Hou[1]

[1]Department of Radiology, Shengjing Hospital of China Medical University, Shenyang, China; [2]Department of Orthopedics, Shengjing Hospital of China Medical University, Shenyang, China; [3]CT Clinical Science, Philips Healthcare, Shenyang, China; [4]Department of Pathology, Shengjing Hospital of China Medical University, Shenyang, China

Contributions: (I) Conception and design: T Wang, Z Fan; (II) Administrative support: Y Hou; (III) Provision of study materials or patients: T Wang, Z Fan, Y Yue; (IV) Collection and assembly of data: T Wang, Y Yue, X Deng; (V) Data analysis and interpretation: T Wang, Z Fan, X Lu, X Deng, Y Hou; (VI) Manuscript writing: All authors; (VII) Final approval of manuscript: All authors.

Correspondence to: Yang Hou, MD. Department of Radiology, Shengjing Hospital of China Medical University, No. 36, Sanhao Street, Heping District, Shenyang 110004, China. Email: houyang_sj@126.com.

Background: Programmed death ligand-1 (*PD-L1*) expression serves a predictive biomarker for the efficacy of immune checkpoint inhibitors (ICIs) in the treatment of patients with early-stage lung adenocarcinoma (LA). However, only a limited number of studies have explored the relationship between *PD-L1* expression and spectral dual-layer detector-based computed tomography (SDCT) quantification, qualitative parameters, and clinical biomarkers. Therefore, this study was conducted to clarify this relationship in stage I LA and to develop a nomogram to assist in preoperative individualized identification of *PD-L1*-positive expression.

Methods: We analyzed SDCT parameters and *PD-L1* expression in patients diagnosed with invasive nonmucinous LA through postoperative pathology. Patients were categorized into *PD-L1*-positive and *PD-L1*-negative expression groups based on a threshold of 1%. A retrospective set (N=356) was used to develop and internally validate the radiological and biomarker features collected from predictive models. Univariate analysis was employed to reduce dimensionality, and logistic regression was used to establish a nomogram for predicting *PD-L1* expression. The predictive performance of the model was evaluated using receiver operating characteristic (ROC) curves, and external validation was performed in an independent set (N=80).

Results: The proportions of solid components and pleural indentations were higher in the *PD-L1*-positive group, as indicated by the computed tomography (CT) value, CT at 40 keV (CT40keV; a/v), electron density (ED; a/v), and thymidine kinase 1 (TK1) exhibiting a positive correlation with *PD-L1* expression. In contrast, the effective atomic number (Zeff; a/v) showed a negative correlation with *PD-L1* expression [r=−0.4266 (Zeff. a), −0.1131 (Zeff.v); P<0.05]. After univariate analysis, 18 parameters were found to be associated with *PD-L1* expression. Multiple regression analysis was performed on significant parameters with an area under the curve (AUC) >0.6, and CT value [AUC =0.627; odds ratio (OR) =0.993; P=0.033], CT40keV.a (AUC =0.642; OR =1.006; P=0.025), arterial Zeff (Zeff.a) (AUC =0.756; OR =0.102; P<0.001), arterial ED (ED.a) (AUC =0.641; OR =1.158, P<0.001), venous ED (ED.v) (AUC =0.607; OR =0.864; P<0.001), TK1 (AUC =0.601; OR =1.245; P=0.026), and diameter of solid components (Dsolid) (AUC =0.632; OR =1.058; P=0.04) were found to be independent risk factors for PD-L1 expression in stage I LA. These seven predictive factors were integrated into the development of an SDCT parameter-clinical nomogram, which demonstrated satisfactory discrimination ability in the training set [AUC =0.853; 95% confidence interval (CI): 0.76–0.947], internal validation set (AUC =0.824; 95% CI: 0.775–0.874), and external validation set (AUC =0.825; 95% CI: 0.733–0.918). Decision curve analyses also revealed the highest net benefit for the nomogram across a broad threshold probability range (20–80%), with a clinical impact curve (CIC) indicating its clinical validity.

Comparisons with other models demonstrated the superior discriminatory accuracy of the nomogram over any individual variable (all P values <0.05).

Conclusions: Quantitative parameters derived from SDCT demonstrated the ability to predict for *PD-L1* expression in early-stage LA, with Zeff.a being notably effective. The nomogram established in combination with TK1 showed excellent predictive performance and good calibration. This approach may facilitate the improved noninvasive prediction of *PD-L1* expression.

Keywords: Spectral computed tomography (spectral CT); programmed death ligand-1 (*PD-L1*); invasive lung adenocarcinoma (invasive LA); thymidine kinase 1 (TK1); prediction model

Introduction

With over 2 million people being diagnosed with lung cancer every year, this disease is a global health concern and the leading cause of cancer-related death worldwide (1). Non-small cell lung cancer (NSCLC) accounts for 80–85% of lung cancer cases, and adenocarcinoma is the most common NSCLC subtype, accounting for approximately 47% of cases in Western patients and 55–60% in Chinese patients (2).

In patients with stage I adenocarcinoma and no contraindications, complete surgical resection should be performed. Nevertheless, in cases of multiple cancerous foci that cannot be simultaneously removed, or if the patient is in poor health, other possible treatments need to be considered. Molecular targeted therapy is limited to patients with certain gene mutations. Cheng *et al.* (3) reported that drugs targeting epidermal growth factor receptor (*EGFR*) mutations are 33.3% effective for the treatment of multifocal ground-glass opacity (GGO), citing the reason for this low effectiveness rate being the heterogeneity of gene mutation between multiple primary lung cancers.

Immune checkpoint inhibitors (ICIs) have enabled a new paradigm for early-stage lung cancer treatment, with programmed death ligand-1 (*PD-L1*) inhibitors being the most widely used and demonstrating significant clinical benefits for treating NSCLC.

PD-L1 expression has been approved by the US Food and Drug Administration (FDA) as a predictive biomarker for ICI efficacy (4). Early tumors exhibit strong host antitumor immune adaptability and low tumor clone heterogeneity. ICIs can boost antitumor effects in the early or even preinvasive stages by blocking the *PD-L1/PD-1* pathway (5). A *PD-L1* level of ≥1% has been positively correlated with the major pathological response (MPR), pathological complete response (PCR), 3-year overall survival (OS), and disease-free survival (DFS) rates in patients treated with neoadjuvant immunotherapy (6,7). Xu *et al.* (8) reported that ICIs exhibit good safety and efficacy in patients with lung adenocarcinoma (LA) featuring multiple ground-glass nodules. These preliminary findings suggest the potential of adjuvant immunotherapy in treating early-stage adenocarcinomas.

Traditionally, the detection of *PD-L1* expression has relied on pathological puncture biopsies or resected specimens, which are invasive procedures that involve high complication rates and specialized materials while being limited in providing dynamic monitoring. Therefore, a more precise, less intrusive, and cost-effective prediction method is needed.

High-resolution computed tomography (HRCT) and positron emission tomography (PET) have improved the detection rates for early adenocarcinoma, and studies have reported correlations between HRCT imaging characteristics, PET metabolic parameters, and *PD-L1* expression. Nevertheless, these parameters display dubious diagnostic performance, showing only moderate sensitivity/specificity of 64.7–83% (9,10). Several studies have focused on the noninvasive prediction of *PD-L1* expression and generated promising computed tomography (CT) or PET/CT-based radiomics models; however, the sample sizes in these studies were small, and most of the patients had advanced NSCLC (11,12).

New-generation spectral dual-layer detector-based computed tomography (SDCT) achieves the conversion and transmission of both high- and low-energy X-rays at the detector level. It can perform simultaneous, isotropic,

homologous, and synchronous imaging, with no requirement for specific scanning modes. Compared with traditional CT, SDCT provides a variety of quantitative analysis tools and comprehensive diagnostic modes based on functional parameters. It can quantify early adenocarcinomas, differentiate between benign and malignant lung tumors, and distinguish histological subtypes (13). Compared with scanners such as dual-source or dual-energy CT and gemstone spectral CT, SDCT has more marked advantages in reducing noise and optimizing image quality. A previous study found there to be a correlation between quantitative SDCT parameters and EGFR mutations in LA (14). normalized iodine density (NID) can enable the prediction of EGFR mutations in NSCLC, whereas slope of spectral curve (λHU) can be employed to predict Ki-67 expression levels (15). SDCT features that correspond to hemodynamic information within tumors may also be useful for assessing changes in the tumor microenvironment. Some studies have examined the correlation between *PD-L1* expression and SDCT parameters and discovered that CT at 40 keV (CT40keV) and CT70keV are elevated in *PD-L1*-positive cases. These parameters can thus be used to quantify *PD-L1* expression in LA (16).

Immunotherapy is promising for the treatment of early-stage LA; however, predicting *PD-L1* expression remains challenging. Moreover, few studies have examined the relationship between *PD-L1* expression and spectral CT quantification, qualitative parameters, and clinical biomarkers. We therefore aimed to determine whether early screening tools could facilitate the prediction of *PD-L1* expression in patients with stage I LA. Additionally, we sought to develop a rapid and innovative noninvasive diagnostic model and nomogram to support personalized treatment approaches. We present this article in accordance with the TRIPOD reporting checklist (available at https:// qims.amegroups.com/article/view/10.21037/qims-24-15/rc).

Methods

Patients and study design

We recruited patients who underwent preoperative enhanced SDCT scanning at Shengjing Hospital of China Medical University between July 2021 and May 2023. The inclusion criteria were as follows: (I) a single lesion ≤40 mm in diameter (on the lung window) and sufficient image quality; (II) preoperative detection of lung cancer tumor markers [carcinoembryonic antigen (CEA), cytokeratin 19 fragment (CYFRA21-1), neuron-specific enolase (NSE), gastrin-releasing peptide precursor (ProGRP)], tumor abnormal protein (TAP), and thymidine kinase 1 (TK1); and (III) postoperative pathological confirmation of stage I LA and immunohistochemical (IHC) determination of *PD-L1* expression level. Meanwhile, the exclusion criteria were the following: (I) multiple GGOs; (II) lymph node or distant metastases; (III) incomplete clinical data or no surgical/ pathological results; and (IV) a history of tumor adjuvant therapy prior to surgery. This retrospective study was approved by the Medical Ethics Committee of Shengjing Hospital of China Medical University (No. 2022PS1055K) and was conducted in accordance with the Declaration of Helsinki (as revised in 2013). Written informed consent was obtained from all patients.

Scanning procedure

All patients underwent a three-phase chest enhanced SDCT scan on an IQon Spectral CT device (Philips, Amsterdam, the Netherlands). Injections of 50–80 mL of iodixanol contrast agent (270 mg/mL; GE HealthCare, Chicago, IL, USA) were administered through the cubital veins and followed by a 20- to 30-mL injection of saline at a flow rate of 3.0 mL/s. Patients were scanned while holding their breath and maintaining calm respiration between scans, and both arterial and venous phase (VP) images were acquired 25 and 60 s after injection.

The acquisition parameters were as follows: 120 kVp, tube current modulation, rotation speed =0.33 sec/rotation, helical pitch =0.671, collimation =64 mm × 0.625 mm, and matrix =512×512. Level of 3 of iDose on recon mode with a standard B filter reviewed in mediastinal windowing, along with Y-detail (YB) for lung windowing, was used to reconstruct spectral base images (SBIs) with a slice thickness of 1 mm and an increment of 1 mm.

Image analysis

Further image analysis was performed using a postprocessing workstation (IntelliSpace Portal Version 6.5, Philips). Regions of interest (ROIs) were delineated in a semiautomated manner (supported by automatic recognition with manual modification) across three consecutive layers centered on the maximum diameter. This was followed by synchronization to CT40keV, CT100keV [monoenergetic (MonoE) at 40 keV and 100 keV], iodine density (ID), effective atomic number (Zeff), and electronic density (ED). The delineation of ROIs

was adjusted to encompass >80% of the targeted lesion, with the large bronchi, blood vessels, and cavities being excluded. The copy-and-paste function was employed to maintain uniformity in the size and positioning of the ROIs between the arterial phase (AP) and VP.

All measurements were independently performed by two senior radiologists with >15 years of experience under double-blind conditions, and the mean values were calculated. The parameters obtained are described below. (I) CT values [Hounsfield unit (HU)] were acquired in plain phase under mixed-energy CT, CT40keV, and CT100keV (MonoE). (II) Slope of the spectral curve (λHU) was calculated as follows: (CT40keV – CT100keV)/(100–40). (III) The ID was normalized to standardize variations in patient hemodynamics and contrast agent dose distribution and was expressed as follows: NID = ID/IDAorta (iodine density of thoracic aorta or subclavian artery in the same layer). (IV) Arterial enhancement fraction (AEF) was calculated as follows: T1/T2 ×100, where T1 is the ID of the artistic phase, and T2 is the ID of the VP.

Lung cancer tumor markers, tumor abnormal protein, and TK1 testing

Peripheral venous blood (5 mL) was extracted after all patients had fasted and was centrifuged at 1,500 g for 15 min, after which qualified serum was extracted. using E601 cobas electrochemical luminescence immunoassay analyzer (Roche Diagnostics, Basel, Switzerland), and the detection reagents were all original matching-qualified kits from Roche. The reference ranges were established as follows: CEA, 0–5 ng/mL; CYFRA21-1, 0.1–3.3 ng/mL; NSE, 0–16.3 ng/mL; and ProGRP, 28.3–65.7 pg/mL.

For TAP detection, blood samples were smeared, air-dried, and then treated with TAP reagents, which were added in dropwise fashion. Subsequently, the mixtures were dried, and then changes in TAP aggregates were observed under a microscope to detect growth areas under a threshold value of 121 μm^2.

For TK1 detection, 3 mL of fasting peripheral venous blood from each patient was centrifuged at 1,000 g for 10 min, the serum was separated using an enzyme-linked immunosorbent assay (ELISA) kit under a threshold of 2 pmol/L according to the manufacturer's instructions.

Pathologic diagnosis and IHC analysis

All specimens were fixed in 4% formaldehyde solution,

embedded in paraffin, sectioned into five consecutive slices with a microtome, and subjected to hematoxylin and eosin (HE) and *PD-L1* IHC staining. IHC was performed using the SP method on the Ventana BenchMark platform (Roche Diagnostics), and *PD-L1* staining results were determined using the SP263 scoring system.

Tumor cell (TC) positivity score TC (+) is the percentage (%) of TCs stained with any intensity of *PD-L1* membrane in all tumor cells, and TC ≥1% was defined as positive expression (second line). Pathological analyses were conducted by two experienced pathologists under double-blind conditions according to the latest International Association for Study of Lung Cancer (IASLC) grading system (17).

Statistical analysis

SPSS v. 26.0 (IBM Corp., Armonk, NY, USA) and MedCalc version 19.6.4 (MedCalc Software, Ostend, Belgium) were used to analyze the distribution of data from each group. Count data are expressed as numbers and percentages, and continuous variables as the mean ± standard deviation or as the medians and interquartile range. Nonnormally distributed data were compared with the Mann-Whitney test and Kruskal-Wallis tests. Normally distributed data were compared using the Student *t*-test or Fisher exact test, and count data were compared using the chi-squared test. The agreement between the two readers' assessments of the parameters was calculated using the intragroup correlation coefficient (ICC).

Diagnostic performance was compared using receiver operating characteristic (ROC) analysis, with the Youden index being used to set the highest performance threshold. Univariate analyses were applied to screen for statistically different variables, with the significant variables [area under the curve (AUC) values >0.6] being selected for multivariate logistic regression analyses (backward stepwise regression). The regression coefficients were used as the variables' weights in the predictive model. Nomograms were plotted using R version 4.2.0 based on the logistic analysis of the independent risk factors. AUC was used to evaluate the model's discriminatory ability. Calibration curves and the Hosmer-Lemeshow test were used to assess the goodness of fit of the nomogram, and decision curve analysis (DCA) was used to determine the clinical effectiveness of the nomogram via the calculation of net benefits under different threshold probabilities (18). Model comparisons between the AUC values were performed using the Delong test.
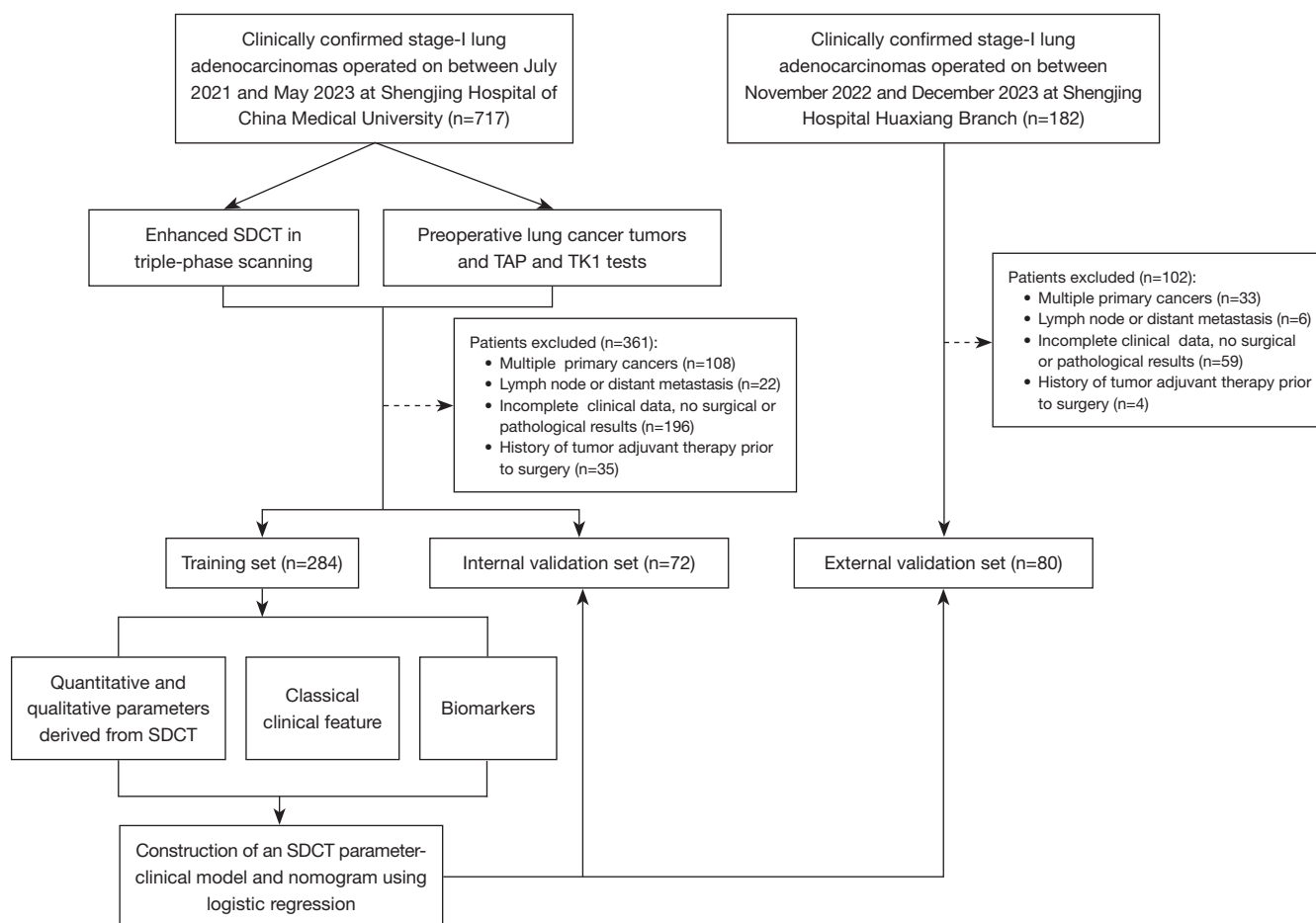
Figure 1 Flowchart of participant selection. SDCT, spectral dual-layer detector-based computed tomography; TAP, tumor abnormal protein; TK1, thymidine kinase 1.

Statistical significance was set at a P value <0.05.

Results

Study population and baseline analysis

A total of 356 participants (119 men and 237 women; median age 63 years; age range, 33–85 years) included in this study were divided into negative (n=202) and positive (n=154) groups according to *PD-L1* expression. A flowchart of the patient selection process is shown in *Figure 1*. Eighty percent of the cases (n=284) were randomly assigned to the training set, while the remaining 20% of cases (n=72) were assigned to the internal validation set. In addition, 80 cases from Shengjing Hospital Huaxiang Branch were included in the independent external validation set. *Table 1* summarizes the CT characteristics, SDCT parameters, and

clinical biomarker results of the patients. All parameters were balanced between the training and validation sets (all P value >0.05).

Excluding sex, age, average diameter (Daverage), international bronchial morphology, vacuole sign, margin, and ID/NID.v, venous slope of spectral curve (λHU.v), AEF, CYFRA21-1, NSE, ProGRP, and TAP, the remaining factors differed significantly between the negative and positive *PD-L1* expression groups (all P values <0.05). The proportions of solid components [mix GGO (mGGO), diameter of solid components (Dsolid)] and pleural indentations were higher in the *PD-L1*-positive group, with CT value, CT40keV (a/v), CT100keV (a/v), electron density (ED) (a/v), arterial slope of spectral curve (λHU.a), CEA, and TK1 showing a positive correlation with *PD-L1* expression and Zeff (a/v) showing a negative correlation [r=−0.4266 (Zeff.a), −0.1131 (Zeff.v); P<0.05].

Table 1 Baseline characteristics of PD-L1 expression in the training and validation sets

Characteristics	All (N=356)	Negative group (N=202)	Positive group (N=154)	P1	Training set (N=284)	Internal validation set (N=72)	P2	External validation set (N=80)
Sex				0.5			0.473	
Women	237 (66.6)	131 (64.9)	106 (68.8)		186 (65.5)	51 (70.8)		34 (42.50)
Men	119 (33.4)	71 (35.1)	48 (31.2)		98 (34.5)	21 (29.2)		46 (57.50)
Age (years)	63.0 [56.0; 68.2]	63.0 [57.0; 68.0]	61.0 [55.0; 68.8]	0.106	63.0 [56.0; 68.0]	62.5 [56.5; 69.0]	0.805	62.96 (8.23)
Location				0.032			0.411	
LLL	50 (14.0)	24 (11.9)	26 (16.9)		35 (12.3)	15 (20.8)		14 (17.50)
LUL	88 (24.7)	58 (28.7)	30 (19.5)		69 (24.3)	19 (26.4)		23 (28.75)
RLL	61 (17.1)	26 (12.9)	35 (22.7)		50 (17.6)	11 (15.3)		16 (20.00)
RML	24 (6.74)	13 (6.44)	11 (7.14)		20 (7.04)	4 (5.56)		3 (3.75)
RUL	133 (37.4)	81 (40.1)	52 (33.8)		110 (38.7)	23 (31.9)		24 (30.00)
GGO status				0.003			0.124	
0	81 (22.8)	58 (28.7)	23 (14.9)		70 (24.6)	11 (15.3)		
1	275 (77.2)	144 (71.3)	131 (85.1)		214 (75.4)	61 (84.7)		
Margin				0.053			0.935	
0	53 (14.9)	37 (18.3)	16 (10.4)		43 (15.1)	10 (13.9)		3 (3.75)
1	303 (85.1)	165 (81.7)	138 (89.6)		241 (84.9)	62 (86.1)		77 (96.25)
Internal bronchial morphology				0.07			0.378	
0	164 (46.1)	102 (50.5)	62 (40.3)		127 (44.7)	37 (51.4)		52 (65.00)
1	192 (53.9)	100 (49.5)	92 (59.7)		157 (55.3)	35 (48.6)		28 (35.00)
Internal vascular morphology				0.042			0.874	
0	119 (33.4)	77 (38.1)	42 (27.3)		96 (33.8)	23 (31.9)		27 (33.75)
1	237 (66.6)	125 (61.9)	112 (72.7)		188 (66.2)	49 (68.1)		53 (66.25)
Pleural indentation				0.021			0.147	
0	117 (32.9)	77 (38.1)	40 (26.0)		99 (34.9)	18 (25.0)		34 (42.50)
1	239 (67.1)	125 (61.9)	114 (74.0)		185 (65.1)	54 (75.0)		46 (57.50)
Vacuole sign				0.225			0.451	
0	304 (85.4)	177 (87.6)	127 (82.5)		240 (84.5)	64 (88.9)		75 (93.75)
1	52 (14.6)	25 (12.4)	27 (17.5)		44 (15.5)	8 (11.1)		5 (6.25)
Daverage (mm)	17.6 [13.5; 22.6]	17.2 [13.2; 21.8]	18.8 [14.8; 24.9]	0.05	17.9 [14.0; 22.5]	17.0 [12.9; 22.7]	0.62	20.97 (5.02)
Dsolid (mm)	8.91 [3.77; 14.2]	7.85 [0.00; 11.9]	10.6 [5.81; 16.0]	<0.001	8.75 [0.00; 13.7]	9.38 [5.79; 15.4]	0.12	14.76 (5.00)
CT value (HU)	−282.60 [−431.28; −153.90]	−352.65 [−493.50; −176.05]	−233.35 [−378.37; −139.20]	<0.001	−289.55 [−455.02; −162.52]	−226.85 [−390.72; −143.62]	0.053	−164.45 [−212.98; −150.23]

Table 1 (*continued*)

Table 1 (*continued*)

Characteristics	All (N=356)	Negative group (N=202)	Positive group (N=154)	P1	Training set (N=284)	Internal validation set (N=72)	P2	External validation set (N=80)
λHU.a	1.64 [1.07; 2.26]	1.58 [0.99; 2.20]	1.71 [1.15; 2.39]	0.046	1.64 [1.03; 2.28]	1.65 [1.12; 2.23]	0.819	1.86 (0.80)
ID.a	1.70 [1.28; 2.23]	1.66 [1.26; 2.07]	1.87 [1.33; 2.33]	0.019	1.69 [1.27; 2.19]	1.79 [1.34; 2.30]	0.237	1.75 [1.31; 2.29]
ID.aorta.a	10.2 [9.13; 11.4]	10.6 [9.34; 11.6]	9.89 [8.86; 11.2]	0.012	10.2 [9.09; 11.5]	10.4 [9.45; 11.3]	0.525	10.37 (2.15)
NID.a	0.16 [0.13; 0.21]	0.15 [0.12; 0.20]	0.18 [0.14; 0.23]	0.001	0.16 [0.13; 0.21]	0.16 [0.13; 0.22]	0.49	0.17 [0.14; 0.22]
CT40keV.a	−167.25 [−331.22; −55.53]	−218.00 [−386.00; −90.30]	−103.85 [−252.15; −34.15]	<0.001	−171.80 [−337.80; −63.48]	−129.05 [−275.60; −33.15]	0.062	−91.65 [−126.05; −72.45]
CT100keV.a	−265.55 [−410.75; −145.72]	−313.85 [−456.98; −174.90]	−217.35 [−345.67; −118.57]	<0.001	−281.25 [−426.25; −146.95]	−225.25 [−352.25; −144.00]	0.095	−190.40 [−232.10; −170.00]
Zeff.a	8.64 (0.47)	8.81 (0.40)	8.41 (0.46)	<0.001	8.65 (0.48)	8.59 (0.45)	0.384	8.25 (0.41)
ED.a	64.9 [48.2; 82.5]	60.5 [45.2; 73.2]	73.7 [52.8; 88.2]	<0.001	63.6 [46.5; 82.4]	66.4 [52.4; 83.8]	0.427	62.55 [53.38; 76.95]
CT40keV.v	−196.30 [−350.35; −56.42]	−222.15 [−357.60; −75.07]	−120.35 [−310.08; −34.15]	<0.001	−196.90 [−354.17; −58.45]	−172.05 [−318.90; −53.95]	0.37	−38.85 [−98.92; −19.70]
CT100keV.v	−302.80 [−442.90; −155.90]	−354.15 [−476.72; −191.20]	−244.45 [−408.92; −131.08]	0.001	−322.00 [−459.78; −155.45]	−290.20 [−408.17; −172.40]	0.56	−148.58 (69.39)
ID.v	1.61 [1.25; 2.02]	1.61 [1.28; 1.96]	1.62 [1.22; 2.05]	0.86	1.59 [1.25; 2.02]	1.62 [1.30; 1.94]	0.64	2.45 [2.00; 2.98]
ID.aorta.v	4.21 [3.30; 4.90]	4.34 [3.32; 5.05]	4.12 [3.22; 4.66]	0.03	4.20 [3.22; 4.85]	4.35 [3.56; 4.92]	0.102	4.08 (0.38)
NID.v	0.39 [0.30; 0.51]	0.39 [0.31; 0.48]	0.40 [0.29; 0.55]	0.424	0.39 [0.31; 0.51]	0.39 [0.29; 0.51]	0.667	0.59 [0.51; 0.70]
λHU.v	1.69 [1.20; 2.16]	1.65 [1.19; 2.11]	1.74 [1.21; 2.20]	0.416	1.65 [1.18; 2.13]	1.90 [1.35; 2.21]	0.234	1.55 [0.73; 2.15]
Zeff.v	8.57 [8.24; 8.83]	8.64 [8.32; 8.88]	8.47 [8.19; 8.75]	0.002	8.59 [8.25; 8.84]	8.47 [8.18; 8.75]	0.123	7.68 (0.38)
ED.v	65.0 [47.9; 80.3]	59.8 [44.4; 74.2]	70.8 [52.5; 83.4]	0.001	65.0 [46.7; 80.3]	67.3 [52.9; 78.9]	0.555	77.54 (6.84)
AEF	1.09 [1.04; 1.18]	1.10 [1.05; 1.19]	1.09 [1.03; 1.18]	0.265	1.10 [1.04; 1.17]	1.09 [1.05; 1.19]	0.535	0.72 [0.65; 0.76]
CEA	2.26 [1.48; 4.02]	2.03 [1.42; 3.42]	2.76 [1.65; 5.18]	0.002	2.27 [1.47; 4.03]	2.26 [1.59; 4.02]	0.64	2.12 [1.62; 4.21]
CYFRA21-1	2.46 [1.83; 3.21]	2.36 [1.76; 3.11]	2.55 [1.94; 3.27]	0.065	2.41 [1.79; 3.22]	2.58 [2.01; 3.12]	0.233	2.50 [1.94; 3.27]
NSE	14.3 [12.6; 16.3]	14.1 [12.6; 16.2]	14.4 [12.7; 16.6]	0.481	14.3 [12.6; 16.3]	14.2 [12.6; 16.2]	0.551	13.50 [11.60; 15.54]
ProGRP	44.5 [37.0; 54.9]	43.5 [36.7; 53.1]	45.3 [38.1; 60.7]	0.06	44.1 [36.9; 54.7]	45.3 [37.3; 56.1]	0.412	42.16 [38.36; 53.11]
TAP	124 [104; 136]	119 [102; 135]	126 [106; 137]	0.086	124 [104; 136]	122 [100; 136]	0.533	125.98 [113.83; 132.24]
TK1	0.99 [0.28; 2.14]	0.84 [0.22; 1.63]	1.27 [0.35; 2.22]	0.001	0.99 [0.31; 2.03]	0.88 [0.22; 2.20]	0.927	0.63 [0.19; 2.21]

Continuous variables are presented as median and interquartile range [P25, P75] or mean (standard deviation); categorical variables are presented as n (%). P1, P value of negative group vs. positive group; P2, P value of training set vs. internal validation set. PD-L1, programmed death ligand 1; LLL, left lower lobe; LUL, left upper lobe; RLL, right lower lobe; RML, right middle Lobe; RUL, right upper lobe; GGO, ground-glass opacity; Daverage, average diameter; Dsolid, diameter of solid components; CT, computed tomography; HU, Hounsfield unit; λHU.a, arterial slope of spectral curve; ID.a, arterial iodine density; ID.aorta.a, arterial iodine density of thoracic aorta; NID.a, normalized arterial iodine density; CT40keV.a, arterial CT 40 keV; CT100keV.a, arterial CT 100 keV; Zeff.a, arterial effective atomic number; ED.a, arterial electronic density; CT40keV.v, venous CT 40 keV; CT100keV.v, venous CT 100 keV; ID.v, venous iodine density; ID.aorta.v, venous iodine density of thoracic aorta; NID.v, normalized venous iodine density; λHU.v, venous slope of spectral curve; Zeff.v, venous effective atomic number; ED.v, venous electronic density; AEF, arterial enhancement fraction; CEA, carcinoembryonic antigen; CYFRA21-1, cytokeratin 19 fragment; NSE, neuron-specific enolase; ProGRP, gastrin-releasing peptide precursor; TAP, tumor abnormal protein; TK1, thymidine kinase 1.

Construction and assessment of the SDCT parameter-clinical nomogram in the training set and validation set

Most of the measured metrics differed significantly according to *PD-L1* expression. In the univariate regression analysis, 18 parameters were found to be associated with *PD-L1* expression (*Table 2*). To construct our nomogram, multiple regression analysis was performed on any parameters with AUCs of >0.6. After multicollinearity variables were excluded, CT values (P=0.033), CT40keV.a (P=0.025), arterial effective atomic number (Zeff.a), arterial electronic density (ED.a), venous electronic density (ED.v) (all P values <0.001), TK1 (P=0.026), and Dsolid (P=0.04) were identified as independent risk factors for *PD-L1* expression in patients with stage I LA (*Table 2*).

We combined the above parameters to establish our nomogram, as shown in *Figure 2*; by adding the scores on the top axis that corresponded to each risk factor, we calculated the total score and corresponding risk coefficient on the bottom axis. The risk prediction probability can be determined by first drawing a vertical line on the point axis in the nomogram to obtain the individual points corresponding to each parameter at different values. This operation should be repeated for each variable, with the scores of all parameters being summed to obtain the total value. Subsequently, a vertical line should be drawn downward to obtain the final risk prediction probability of *PD-L1*-positive expression for a given patient.

The nomogram showed good discrimination, with an AUC of 0.853 [95% confidence interval (CI): 0.76–0.947] in the training set (*Figure 3A*). It was internally validated using 500 bootstrap replicates and fivefold cross-validation. When the optimal cutoff was set to 0.54, the corresponding sensitivity, specificity, positive likelihood ration (PLR), and negative likelihood ratio (NLR) were 80%, 81%, 4.2, and 0.247, respectively. Through internal and external validation sets, it was confirmed that this nomogram model had satisfactory performance in identifying *PD-L1* expression. In the internal validation set, the AUC was 0.824 (95% CI: 0.775–0.874; *Figure 3B*). Its sensitivity, specificity, PLR, and NLR values were 63.7%, 88.7%, 5.663, and 0.409, respectively, when the optimal cutoff point was 0.525. In the external validation set, the AUC was 0.825 (95% CI: 0.733–0.918; *Figure 3C*). When the optimal cutoff point was set to 0.373, the corresponding sensitivity, specificity, PLR, and NLR values were 94.4%, 65.9%, 2.77, and 0.084, respectively.

Calibration curves indicated good agreement between the model's predictions and actual observations (*Figure 4A*). The P value obtained using the Hosmer-Lemeshow test was not significant (0.679), indicating good calibration. In addition, a strong calibration performance was also demonstrated in both the internal and external validation sets (*Figure 4B,4C*). The P values from the Hosmer-Lemeshow test were not significant, with values of 0.254 and 0.399, respectively, indicating that there was no significant difference between the predicted and the actual probability.

The clinical decision curve for the training set is shown in *Figure 5A*. Both DCA and fivefold cross-validation showed that using the nomogram to determine *PD-L1* expression could provide more net benefit than using a regimen with all or none of the parameters if the threshold probability was between 20% and 80%. DCAs showed a higher net gain both in the internal and external validation sets when the threshold probability was 20–80% (*Figure 5B,5C*). Clinical impact curve (CIC) analysis confirmed the clinical effectiveness of the nomogram. When the threshold probability was >50%, those with positive *PD-L1* expression population were closely aligned with the actual population, confirming the nomogram's clinical efficacy (*Figure 6A*). The CIC analysis also indicated the model's high clinical validity both in the internal and external validation sets (*Figure 6B,6C*).

Model comparisons

The Delong test was employed to compare our nomogram with each of the variables it included, and *Figure 7* shows the results of ROC analysis. We found high discriminatory accuracy and superior predictive capability for *PD-L1* expression compared to any single variable used alone (all P values <0.05). The holistic nomogram exhibited optimal discriminatory ability when compared with the modified nomograms that each had a parameter removed (*Table 3*).

Discussion

In this study, we combined quantitative and qualitative SDCT parameters, clinical features, and biomarkers to predict *PD-L1* expression in stage I LA (*Figure 8*). Our findings revealed that CT.value, CT40keV.a, Zeff.a, ED.a, ED.v, TK1, and Dsolid (all P values <0.05) were independent risk factors for *PD-L1* expression, with Zeff.a and ED.a showing high diagnostic efficacy and sensitivity/specificity. An SDCT parameter-clinical nomogram was subsequently established based on these parameters, which

Table 2 Univariate and multivariate logistic regression analysis of SDCT parameters and clinical candidate biomarkers in the training set

Characteristics	Univariate					Multivariate				
	B	SE	OR (95% CI)	Z	P	B	SE	OR (95% CI)	Z	P
TK1	0.213	0.08342	1.238 (1.059–1.471)	2.557	0.011	0.219	0.10708	1.245 (1.021–1.55)	2.044	0.026
Internal vascular morphology	0.383	0.25653	1.467 (0.89–2.438)	1.493	0.135					
ProGRP	0.016	0.00883	1.016 (0.999–1.034)	1.82	0.069					
TAP	0.007	0.00483	1.007 (0.998–1.017)	1.5	0.134					
NSE	0.035	0.02978	1.036 (0.977–1.099)	1.175	0.24					
CT100keV.v	0.002	0.00065	1.002 (1–1.003)	2.653	0.008					
CYFRA21.1	0.195	0.08566	1.216 (1.042–1.458)	2.282	0.022					
CEA	0.017	0.01337	1.017 (0.999–1.055)	1.297	0.195					
AEF	0.082	0.39439	1.086 (0.488–2.386)	0.209	0.835					
ED.v	0.014	0.00592	1.014 (1.002–1.026)	2.291	0.022	−0.146	0.03735	0.864 (0.799–0.926)	−3.913	<0.001
Zeff.v	−0.265	0.24701	0.767 (0.469–1.24)	−1.072	0.284					
λHU.v	0.033	0.10864	1.034 (0.835–1.297)	0.304	0.761					
NID.v	1.115	0.74124	3.05 (0.717–13.25)	1.504	0.132					
ID.aorta.v	−0.221	0.12452	0.801 (0.626–1.021)	−1.778	0.075					
ID.v	0.059	0.22024	1.06 (0.687–1.635)	0.266	0.79					
NID.a	5.14	1.90669	170.7 (4.383–7,959)	2.696	0.007					
CT40keV.v	0.002	0.00062	1.002 (1–1.003)	2.636	0.008					
ED.a	0.019	0.00584	1.02 (1.008–1.032)	3.321	0.001	0.147	0.03645	1.158 (1.083–1.25)	4.026	<0.001
Zeff.a	−2.158	0.33374	0.116 (0.058–0.216)	−6.467	< 0.001	−2.284	0.39503	0.102 (0.045–0.213)	−5.782	<0.001
ID.aorta.a	0.009	0.01262	1.009 (0.989–1.066)	0.726	0.468					
Location LUL	−0.622	0.42084	0.537 (0.233–1.222)	−1.479	0.139					
Location RLL	0.184	0.44221	1.202 (0.504–2.874)	0.416	0.677					
Location RML	−0.258	0.56249	0.773 (0.252–2.326)	−0.458	0.647					
Location RUL	−0.463	0.3902	0.63 (0.291–1.355)	−1.186	0.236					
ID.a	0.345	0.19372	1.412 (0.968–2.074)	1.779	0.075					
Pleural indentation	0.594	0.25775	1.811 (1.098–3.023)	2.304	0.021					
CT100keV.a	0.002	0.00067	1.002 (1.001–1.004)	3.511	<0.001					
λHU.a	0.318	0.12875	1.374 (1.074–1.782)	2.467	0.014					
CT40keV.a	0.003	0.00066	1.003 (1.001–1.004)	3.795	<0.001	0.006	0.00278	1.006 (1.001–1.012)	2.306	0.025
CT value	0.002	0.00068	1.002 (1.001–1.004)	3.262	0.001	−0.007	0.00305	0.993 (0.987–0.999)	−2.221	0.033
Vacuole sign	0.41	0.32893	1.507 (0.79–2.889)	1.247	0.212					
Internal bronchial morphology	0.376	0.2424	1.456 (0.907–2.349)	1.55	0.121					
Dsolid	0.056	0.01642	1.057 (1.024–1.093)	3.391	0.001	0.057	0.02625	1.058 (1.006–1.115)	2.154	0.04

Table 2 (*continued*)

5992

Wang et al. Development and validation of a novel nomogram

Table 2 (*continued*)

Characteristics	Univariate					Multivariate				
	B	SE	OR (95% CI)	Z	P	B	SE	OR (95% CI)	Z	P
Margin	0.315	0.34105	1.37 (0.709–2.723)	0.924	0.356					
Daverage	0.029	0.01964	1.029 (0.991–1.07)	1.478	0.139					
GGO character	0.687	0.29158	1.987 (1.133–3.57)	2.355	0.019					
Age	−0.019	0.01259	0.981 (0.957–1.005)	−1.525	0.127					
Sex	0.013	0.25161	1.013 (0.617–1.658)	0.053	0.958					

SDCT, spectral dual-layer detector-based computed tomography; SE, standard error; OR, odds ratio; CI, confidence interval; TK1, thymidine kinase 1; ProGRP, gastrin-releasing peptide precursor; TAP, tumor abnormal protein; NSE, neuron-specific enolase; CT100keV.v, venous CT 100 keV; CYFRA21.1, cytokeratin 19 fragment; CEA, carcinoembryonic antigen; AEF, arterial enhancement fraction; ED.v, venous electronic density; Zeff.v, venous effective atomic number; λHU.v, venous slope of spectral curve; NID.v, normalized venous iodine density; ID.aorta.v, venous iodine density of thoracic aorta; ID.v, venous iodine density; NID.a, normalized arterial iodine density; CT40keV.v, venous CT 40 keV; ED.a, arterial electronic density; Zeff.a, arterial effective atomic number; ID.aorta.a, arterial iodine density of thoracic aorta; LUL, left upper lobe; RLL, right lower lobe; RML, right middle lobe; RUL, right upper lobe; ID.a, arterial iodine density; CT100keV.a, arterial CT 100 keV; λHU.a, arterial slope of spectral curve; CT40keV.a, arterial CT 40 keV; CT, computed tomography; D, diameter; GGO, ground glass opacity.
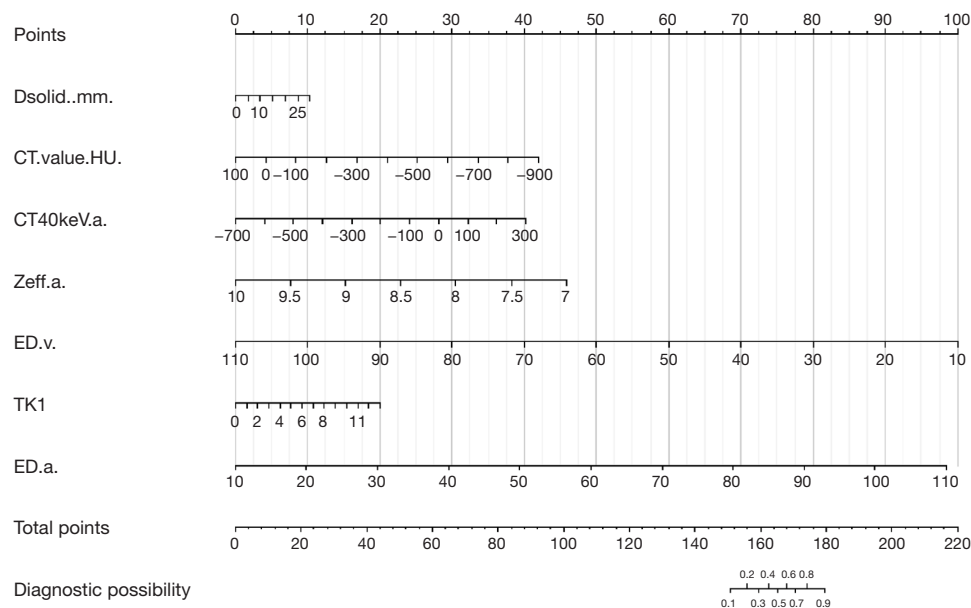
Figure 2 Diagnostic SDCT parameter-clinical nomogram for predicting PD-L1 expression. Dsolid, diameter of solid components; CT, computed tomography; HU, Hounsfield unit; CT40keV.a, arterial CT 40 keV; Zeff.a, arterial effective atomic number; ED.v, venous electronic density; TK1, thymidine kinase 1; ED.a, arterial electronic density; SDCT, spectral dual-layer detector-based computed tomography; PD-L1, programmed death ligand 1.

exhibited superior efficacy compared with individual parameters (P<0.05). The nomogram also demonstrated good diagnostic capability and calibration and can thus potentially aid clinicians in selecting appropriate ICIs for patients with early-stage LA.

PD-L1 ICIs have drastically changed the treatment prospects and prognosis of patients with LA, providing significant clinical benefits for treating NSCLC. ICIs
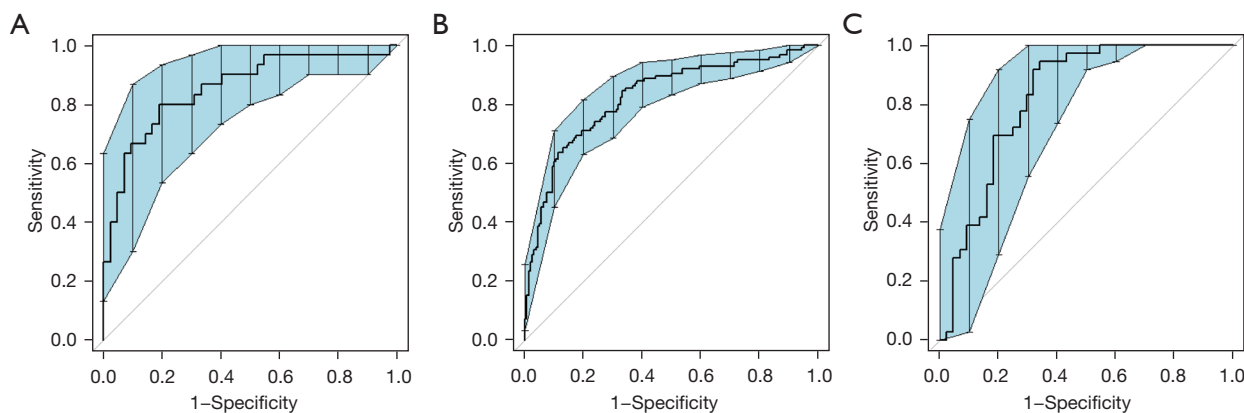
Figure 3 ROC analysis of the SDCT parameter-clinical nomogram for predicting PD-L1 expression in the (A) training set, (B) internal validation set, and (C) external validation set. ROC, receiver operating characteristic; SDCT, spectral dual-layer detector-based computed tomography; PD-L1, programmed death ligand 1.
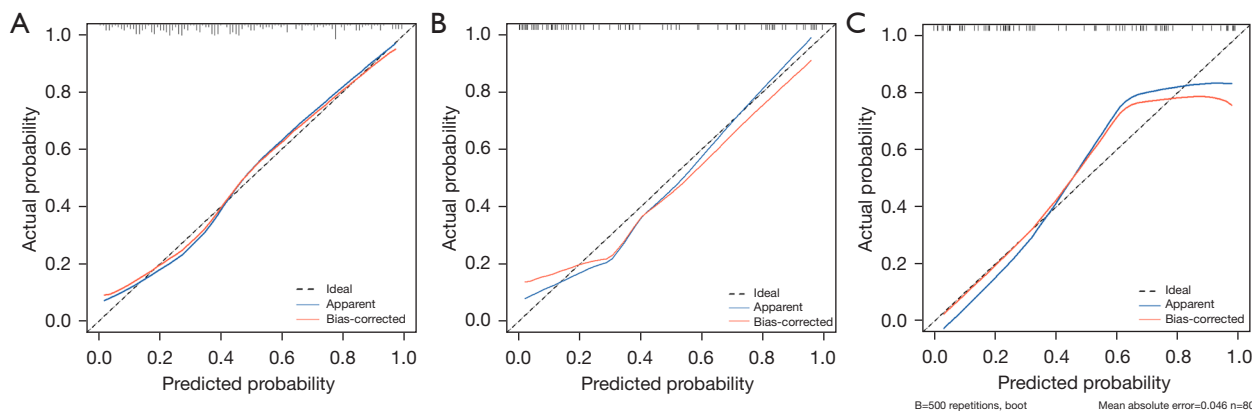

Figure 4 Calibration curve of the SDCT parameter-clinical nomogram in the (A) training set, (B) internal validation set, (C) and external validation set. The horizontal axis represents the predicted probability, and the vertical axis represents the actual occurrence probability. The diagonal dashed line (ideal) in the figure represents the ideal situation where the predicted probability is equal to the actual probability. The blue line (apparent) represents the consistency between the calculated risk probability based on the model and the actual probability. The red line (bias-corrected) refers to the result of self-sampling (bootstrapped 500 times) of the data used to construct the model. SDCT, spectral dual-layer detector-based computed tomography.

significantly prolong the progression-free survival (PFS) and OS of patients compared with chemotherapy. The interaction between *PD-L1* and cancer cell membranes and that between PD-1 and T cells substantially reduces the number of activated T cells, leading to immune evasion by tumor cells (19,20). Therefore, exploring *PD-L1* expression in early-stage LA is crucial to confirming the feasibility of immunotherapy and identifying eligible patients, thus enhancing the personalized treatment for those early-stage tumors and improving patient prognosis.

SDCT not only provides structural information such as lesion size and density but also allows for the tuning of quantitative and functional parameters, particularly Zeff and ED, which have a high sensitivity and specificity for predicting pathological subtypes and aiding in risk stratification in early-stage LA (13,21). We developed a joint model based on SDCT parameters and TK1 for early-stage LA that allowed *PD-L1* expression to be predicted noninvasively (AUCs of 0.853, 0.824, and 0.825 for the training, internal validation, and external validation sets,
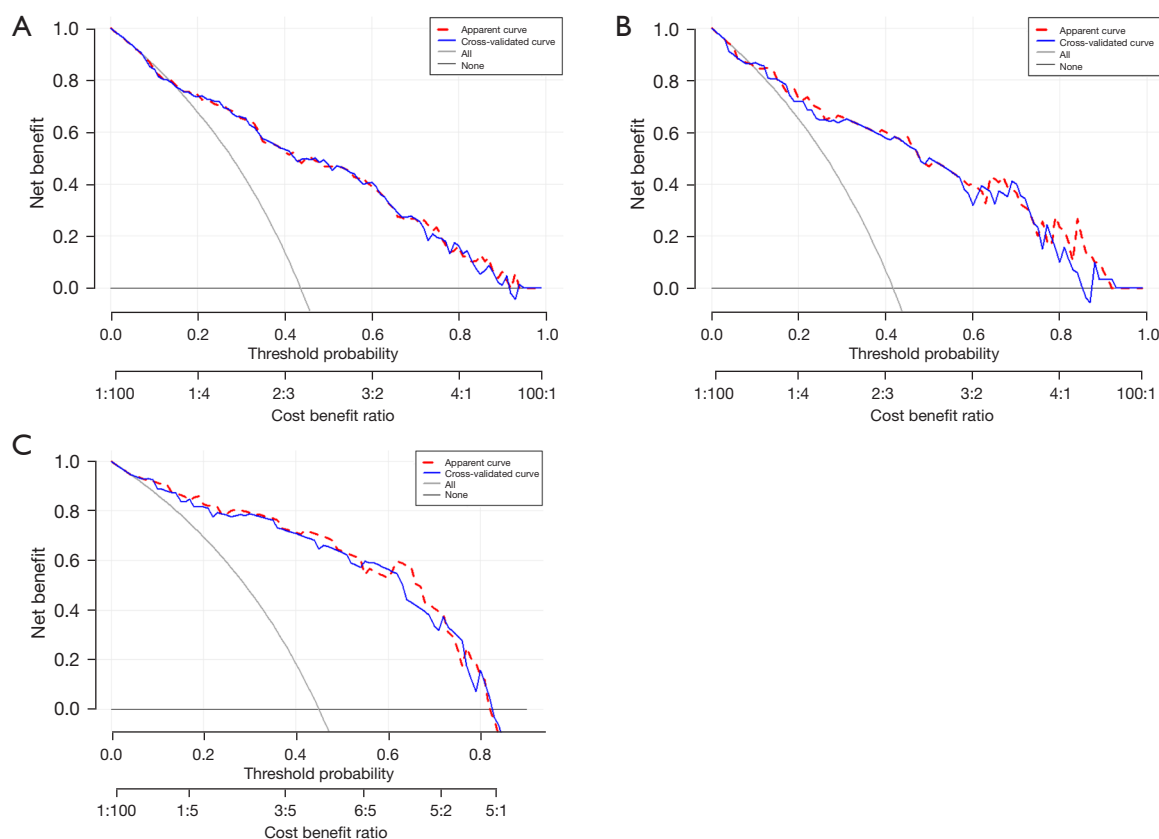
Figure 5 Decision curve analyses for the SDCT parameter-clinical nomogram in the (A) training set, (B) internal validation set, and (C) external validation set. The X-axis represents the threshold probability, the Y-axis represents net benefit, the gray line represents the hypothesis that all patients are PD-L1 positive, the black line represents the hypothesis that all patients are negative, and the red and blue lines represent this column chart and five-fold cross validation, respectively. SDCT, spectral dual-layer detector-based computed tomography; PD-L1, programmed death ligand 1.

respectively). The rate of positive *PD-L1* expression was approximately 43.3% (154/356) in our patient cohort. Pawelczyk *et al.* (22) also found that *PD-L1* was expressed in 32.6% of NSCLC tumors, confirming that immune evasion is important in the early stages of lung cancer, thus laying the foundation for the use of ICIs.

We found that Zeff was lower in the positive group than in the negative group, was negatively correlated with *PD-L1* expression, and exhibited a unique advantage when applied alone (AUC =0.756). When the cutoff was ≤8.47, the specificity (82.18%) and sensitivity (61.04%) indicated a negative relationship between Zeff and LA invasiveness. Zeff can thus be used to monitor changes in lepidic growth components and arrangement structures during tumor cell transformation (13) and to recognize receptor expression earlier. Zeff may represent a quantitative indicator of *PD-L1*

expression in LA. It denotes the average atomic number within the ROI, which can be used to quantitatively analyze the chemical composition of a tumor. Moreover, it can display the distribution of substances in color images, particularly in areas with similar CT values or densities (23); indirectly provide information regarding contrast agent accumulation (24); and has been used to differentiate between LA and squamous cell carcinoma (25). We found that the diagnostic and predictive values of Zeff in the AP were superior to those in the VP. Considering that the tumor vasculature of LA originates from the pulmonary artery and gradually shifts to the bronchial artery as infiltration increases, Zeff.a may be a powerful tool for assessing a tumor's blood supply, histological characteristics, growth pattern, and surrounding microenvironment (25).

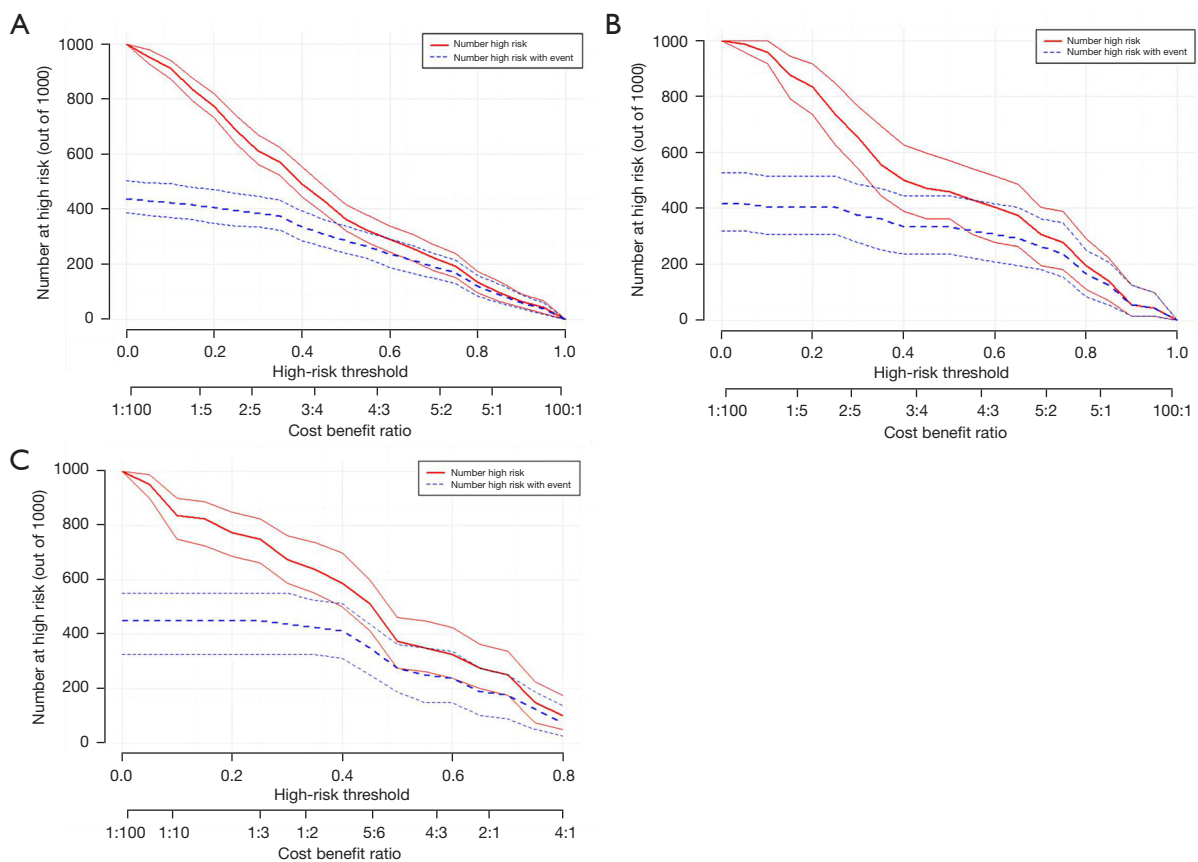We found that ED was positively correlated with *PD-L1*

Figure 6 Clinical impact curve of the SDCT parameter-clinical nomogram in the (A) training set, (B) internal validation set, and (C) external validation set. The horizontal axis represents the risk threshold, the vertical axis represents the number of high-risk individuals per 1,000 individuals, the red line represents the number of individuals identified by the model as being at high risk at different threshold probabilities, and the blue line represents the number of individuals identified by the model as being at high risk at different threshold probabilities and who have actually experienced an outcome event. SDCT, spectral dual-layer detector-based computed tomography.

expression and had a favorable diagnostic performance as an independent predictor of *PD-L1* expression (AUC =0.641). Immune escape occurs more frequently in cancers with higher *PD-L1* expression, decreasing the number of activated T cells and accelerating both carcinogenesis and progression. Increases in relevant SDCT parameters indirectly reflect this transformation through increased intracellular lipids and the enlargement of lymphatic vessels in malignant tumors, resulting in low Zeff and elevated ED (26). ED reflects the relative distribution of the ED corresponding to each voxel ratio to water and does not require CT value conversion. Using this method, the lesion area can be accurately displayed with higher sensitivity than it can on traditional CT (27). Zhang *et al.* (28) proposed that ED can detect more mGGOs and display their infiltrating

components, providing a new method for the preoperative pathological classification of GGOs. Prior research on Zeff and ED has mostly concentrated on identifying benign and malignant pulmonary nodules and their pathological or histological subtypes (13,28,29); however, tumor gene or receptor expression has received less attention.

CT.value reflects the attenuation of X-rays and the density of the tumor tissue and is positively correlated with invasiveness as lepidic-predominant growth decreases and density increases. In our study, CT.value, CT40keV (a/v), and CT100keV (a/v) were higher in the *PD-L1*-positive group. CT40keV.a and CT.value had better predictive values for *PD-L1* expression when the critical values of the two were −184.9 and −284.9 HU, respectively. CT40keV.a (AUC =0.642) and CT value (AUC =0.627) had similar and
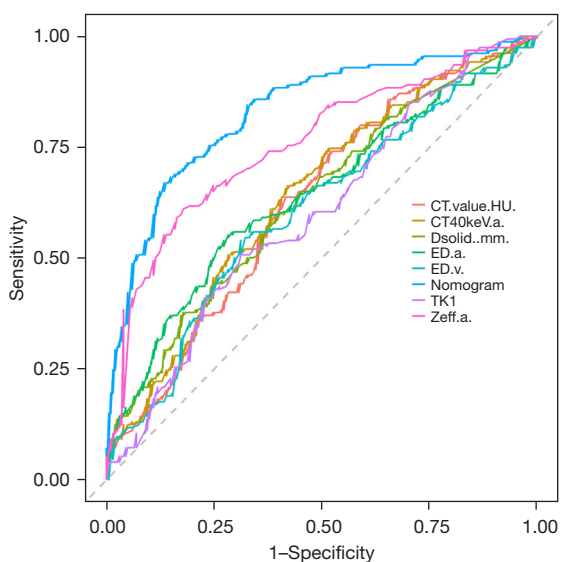
5996

Wang et al. Development and validation of a novel nomogram

Figure 7 Receiver operator characteristic curves of the SDCT parameter-clinical nomogram and other variables incorporated in the nomogram alone, with their discriminatory accuracies for predicting PD-L1 expression being illustrated. This nomogram demonstrated superior diagnostic performance compared with the use of any single parameter alone. CT, computed tomography; HU, Hounsfield unit; CT40keV.a, arterial CT 40 keV; Dsolid, diameter of solid components; ED.a, arterial electronic density; ED.v, venous electronic density; TK1, thymidine kinase 1; Zeff. a, arterial effective atomic number; SDCT, spectral dual-layer detector-based computed tomography; PD-L1, programmed death ligand 1.

well-performing diagnostic efficacies, consistent with the findings of Chen *et al.* (16). The CTV40keV of the *PD-L1*-positive group was larger than that of the negative one, possibly because tumors that express *PD-L1* have more and denser cells with more active cell proliferation and growth; meanwhile, the *PD-L1*-negative group was prone to cystic necrosis, and the tumor cells were packed more loosely. The IQon Spectral CT device uses a unique anticorrelation noise model that ensures low noise and better image quality across 161 energy levels (40–200 keV). We found CT40keV to be an independent predictor of *PD-L1* expression compared with CT100keV. Low-energy images not only enhance tissue enhancement and resolution, making fine anatomical structures and microvascular lesions more distinct, but also enhance the detection of occult foci while reducing the required concentration, flow rate, and total

amount of contrast agent. Chen *et al.* (30) reported that spectral CT parameters indirectly reflect the proliferative activity of LA and that CT40keV is moderately positively correlated with Ki-67.

In our study, higher levels of TK1 and CEA were linked to favorable *PD-L1* expression, suggesting TK1 as a possible biomarker. Adding TK1 to our model improved the predictive performance, which conflicts with the findings of Shi *et al.* (31). They reported that higher CEA and lower CYFRA21-1 levels could predict *PD-L1* expression, but their study used different participants and analyzed GGOs. TK1 is a cell cycle-dependent parameter that can serve as a quantitative marker for cell proliferation. It is involved in DNA precursor synthesis, and its expression level indicates cellular proliferation (32). Serological TK1 can indicate the early development of malignant tumors. TK1 is significantly higher in lung cancers than in benign diseases and its concentration correlates with tumor, node, metastasis (TNM) stage (33). In this study, we demonstrated the association between TK1 and *PD-L1* expression and showed that its diagnostic value was superior to that of TAP or the classical lung cancer markers of CEA, CYFRA21-1, and NSE, confirming its value for predicting receptor expression in patients with early-stage LA. The discriminative ability of TK1 alone is moderate (AUC =0.601), but its accuracy can be greatly improved when combined with other assays, as was confirmed by Shi *et al.* (31).

GGO is a relatively important texture in LA. A solid component on CT may represent alveolar wall collapse, fibrosis, or tumor cell infiltration. In our study, the Dsolid and mGGO rates were higher in the *PD-L1*-positive group, and Dsolid was an independent risk factor for *PD-L1* expression, which is in line with the findings of Wu *et al.* (9) This phenomenon may be explained by the fact that lepidic-predominant adenocarcinomas have a higher prevalence of *PD-L1* expression. This, in turn, correlates with more aggressive subtypes. CT-derived parameters such as size and qualitative features are correlated with the growth and infiltration of early-stage LA (34). We found that internal vascular morphology and pleural indications were correlated with *PD-L1* expression. Further univariate analysis suggested pleural indentation to be a crucial morphological feature of positive *PD-L1* expression. Pleural indentation, a typical feature of invasive adenocarcinoma, is the thickening of the fibrous septa between the tumor and pleural surface. Similarly, Kim *et al.* (35) demonstrated that *PD-L1*-positive adenocarcinomas exhibited radial invasiveness, correlating

Table 3 Comparison of the efficacy of the joint diagnostic models versus that of other variables incorporated in the nomogram used alone for the entire study cohort

Parameter	AUC	Youden	Sensitivity (%)	Specificity (%)	Cutoff
Dsolid	0.632	0.201	59.70	60.40	9.03
CT.value	0.627	0.23	63.60	59.40	−284.9
CT40keV.a	0.642	0.242	66.20	57.90	−184.9
Zeff.a	0.756	0.432	61.04	82.18	8.47
ED.a	0.641	0.27	55.20	71.80	70.5
ED.v	0.607	0.227	53.90	68.80	69.6
TK1	0.601	0.195	50.60	68.80	1.26
Model 1	0.829	0.543	76.9	86.10	0.489
Model 2	0.827	0.579	72.70	85.10	0.468
Model 3	0.821	0.535	66.90	86.60	0.498
Model 4	0.821	0.535	66.90	86.60	0.498
Model 5	0.736	0.379	74.00	63.90	0.404
Model 6	0.79	0.458	67.50	78.20	0.439
Model 7	0.821	0.52	70.80	81.20	0.439
Model 8	0.79	0.458	67.50	78.20	0.439

Model 1: Dsolid + CT.value + CT40keV.a + Zeff.a + ED.v + TK1 + ED.a; Model 2: CT.value + CT40keV.a + Zeff.a + ED.v + TK1 + ED.a; Model 3: Dsolid + CT40keV.a + Zeff.a + ED.v + TK1 + ED.a; Model 4: Dsolid + CT.value + Zeff.a + ED.v + TK1 + ED.a; Model 5: Dsolid + CT.value + CT40keV.a + ED.v + TK1 + ED.a; Model 6: Dsolid + CT.value + CT40keV.a + Zeff.a + TK1 + ED.a; Model 7: Dsolid + CT.value + CT40keV.a + Zeff.a + ED.v + ED.a; Model 8: Dsolid + CT.value + CT40keV.a + Zeff.a + ED.v + TK1. AUC, area under the curve; D, diameter; CT, computed tomography; CT40keV.a, arterial CT 40 keV; Zeff.a, arterial effective atomic number; ED.a, arterial electronic density; ED.v, venous electronic density; TK1, thymidine kinase 1.

with pathological invasiveness, and that *PD-L1*-positive patients experienced worse prognoses. However, in our study revealed, Daverage, internal bronchial morphology, vacuole sign, and margin did not significantly differ between the negative and positive groups, indicating that they were poor predictors of *PD-L1* expression.

Limitations

This study has several limitations which should be noted. First, we employed a retrospective design with inherent patient selection bias and a limited number of cases; consequently, further large-sample studies are warranted

to validate our findings. Second, expanding our research scope to include more advanced radiomics techniques, such as convolutional neural networks, may lead to a better noninvasive prediction of *PD-L1*. Third, all our patients had early-stage LA with relatively homogeneous pathologic types and staging. Including studies with multiple pathologic types and disease stages may enhance the utility of our nomogram.

Conclusions

We examined the quantitative parameters of enhanced SDCT in addition to clinical biomarkers and morphological

5998

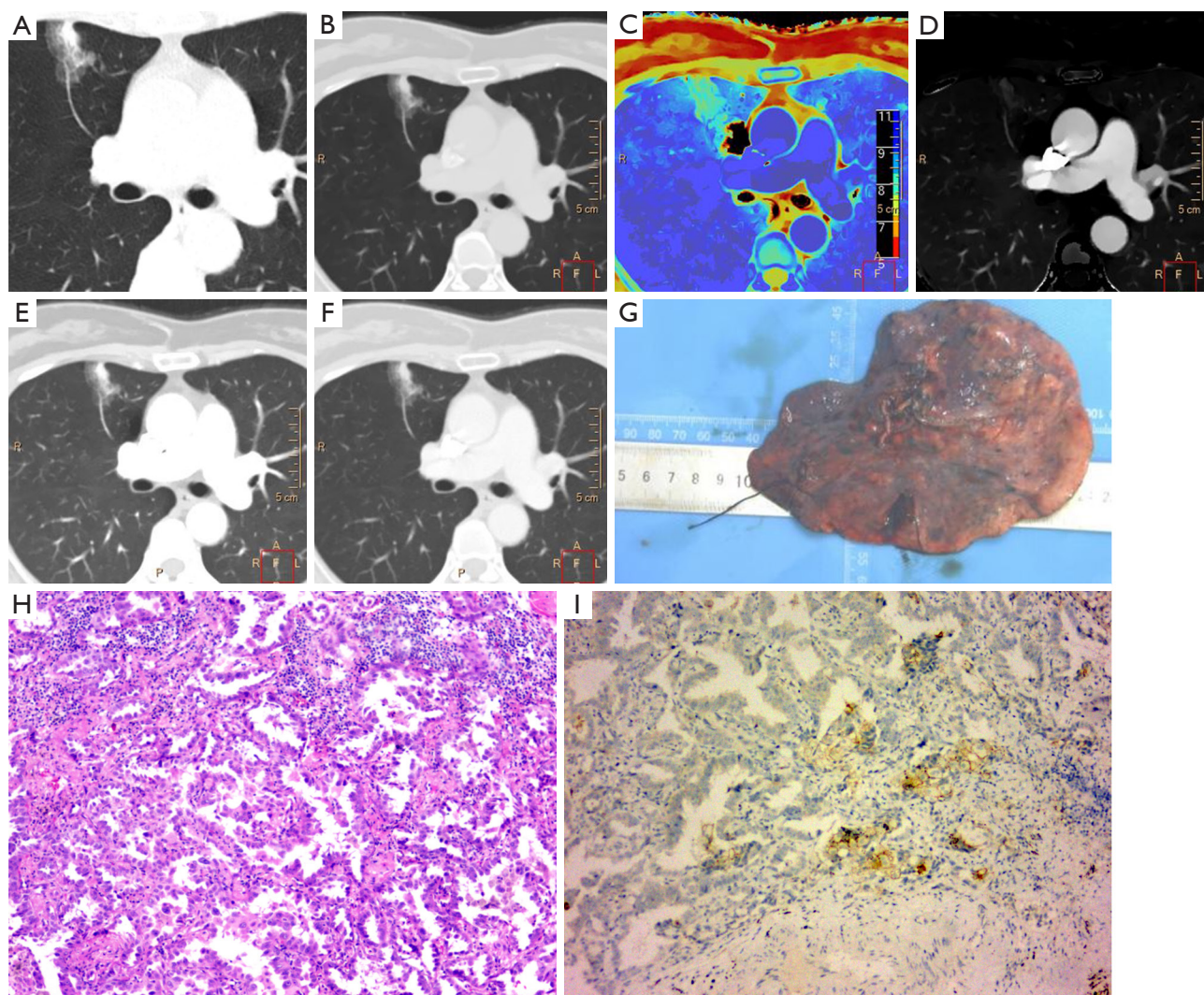Wang et al. Development and validation of a novel nomogram

Figure 8 A 65-year-old female with invasive lung adenocarcinoma in the upper lobe of the right lung, with the lesion manifesting as mixed ground glass and lobulation. (A) CT value of –364.5 HU in the plain phase. (B) Arterial ED =90.4%. (C) Arterial Zeff =8.2. (D) Arterial ID =1.16 mg/mL. (E,F) CT 40 keV and CT 100 keV (MonoE) were –278.2 and –345 HU in the arterial phase and (G,H) for gross and microscopic postoperative pathology (hematoxylin and eosin staining 100×), respectively. (I) Immunohistochemical staining (100×) showing positive PD-LI expression (TC ~5%). The red box represents the direction of the image, making it easy to confirm the location of the lesion, L represents left side, R represents right side. CT, computed tomography; HU, Hounsfield unit; ED, electronic density; Zeff, arterial effective atomic number; ID, iodine density; PD-L1, programmed death ligand 1; TC, tumor cell positive score.

features to predict *PD-L1* expression in LA. Quantitative parameters based on SDCT showed promising capacity to predict *PD-L1* expression in early-stage LAs, particularly Zeff.a. The novel nomogram, when combined with TK1, demonstrated outstanding predictive performance and good calibration, potentially facilitating the noninvasive prediction of *PD-L1* expression.

Acknowledgments

Footnote

Reporting Checklist: The authors have completed the

TRIPOD reporting checklist. Available at https://qims.amegroups.com/article/view/10.21037/qims-24-15/rc

References

1. Siegel RL, Giaquinto AN, Jemal A. Cancer statistics, 2024. CA Cancer J Clin 2024;74:12-49. Erratum in: CA Cancer J Clin 2024;74:203.
2. Chen P, Liu Y, Wen Y, Zhou C. Non-small cell lung cancer in China. Cancer Commun (Lond) 2022;42:937-70.
3. Cheng B, Li C, Zhao Y, Li J, Xiong S, Liang H, Liu Z, Zeng W, Liang W, He J. The impact of postoperative EGFR-TKIs treatment on residual GGO lesions after resection for lung cancer. Signal Transduct Target Ther 2021;6:73.
4. Herbst RS, Giaccone G, de Marinis F, Reinmuth N, Vergnenegre A, Barrios CH, et al. Atezolizumab for First-Line Treatment of PD-L1-Selected Patients with NSCLC. N Engl J Med 2020;383:1328-39.
5. Zhang C, Yin K, Liu SY, Yan LX, Su J, Wu YL, Zhang XC, Zhong WZ, Yang XN. Multiomics analysis reveals a distinct response mechanism in multiple primary lung adenocarcinoma after neoadjuvant immunotherapy. J Immunother Cancer 2021;9:e002312.
6. Deng H, Zhao Y, Cai X, Chen H, Cheng B, Zhong R, Li F, Xiong S, Li J, Liu J, He J, Liang W. PD-L1 expression and Tumor mutation burden as Pathological response biomarkers of Neoadjuvant immunotherapy for Early-stage Non-small cell lung cancer: A systematic review and meta-analysis. Crit Rev Oncol Hematol 2022;170:103582.
7. Zhang F, Guo W, Zhou B, Wang S, Li N, Qiu B, Lv F, Zhao L, Li J, Shao K, Xue Q, Gao S, He J. Three-Year Follow-Up of Neoadjuvant Programmed Cell Death Protein-1 Inhibitor (Sintilimab) in NSCLC. J Thorac Oncol 2022;17:909-20.
8. Xu L, Shi M, Wang S, Li M, Yin W, Zhang J, Zhu J, Jiang F, Xia W, Qiu N, Zhang Z, Huang J, Ma Z, Meng F, Zhu H, Dong G, Wang J, Yin R. Immunotherapy for bilateral multiple ground glass opacities: An exploratory study for synchronous multiple primary lung cancer. Front Immunol 2022;13:1009621.
9. Wu T, Zhou F, Soodeen-Lalloo AK, Yang X, Shen Y, Ding X, Shi J, Dai J, Shi J. The Association Between Imaging Features of TSCT and the Expression of PD-L1 in Patients With Surgical Resection of Lung Adenocarcinoma. Clin Lung Cancer 2019;20:e195-207.
10. Meng N, Fu F, Sun J, Feng P, Luo Y, Wu Y, Li X, Yuan J, Yang Y, Liu H, Wang Z, Wang M. Sensitivity and specificity of amide proton transfer-weighted imaging for assessing programmed death-ligand 1 status in non-small cell lung cancer: a comparative study with intravoxel incoherent motion and (18)F-FDG PET. Quant Imaging Med Surg 2022;12:4474-87.
11. Bracci S, Dolciami M, Trobiani C, Izzo A, Pernazza A, D'Amati G, Manganaro L, Ricci P. Quantitative CT texture analysis in predicting PD-L1 expression in locally advanced or metastatic NSCLC patients. Radiol Med 2021;126:1425-33.
12. Monaco L, De Bernardi E, Bono F, Cortinovis D, Crivellaro C, Elisei F, L'Imperio V, Landoni C, Mathoux G, Musarra M, Pagni F, Turolla EA, Messa C, Guerra L. The "digital biopsy" in non-small cell lung cancer (NSCLC): a pilot study to predict the PD-L1 status from radiomics features of [18F]FDG PET/CT. Eur J Nucl Med Mol Imaging 2022;49:3401-11.
13. Wang T, Yue Y, Fan Z, Jia Z, Yu X, Liu C, Hou Y. Spectral Dual-Layer Computed Tomography Can Predict the

6000

Wang et al. Development and validation of a novel nomogram

Invasiveness of Ground-Glass Nodules: A Diagnostic Model Combined with Thymidine Kinase-1. J Clin Med 2023;12:1107.

14. Zhang G, Cao Y, Zhang J, Zhao Z, Zhang W, Zhou J. Epidermal growth factor receptor mutations in lung adenocarcinoma: associations between dual-energy spectral CT measurements and histologic results. J Cancer Res Clin Oncol 2021;147:1169-78.

15. Lin L, Cheng J, Tang D, Zhang Y, Zhang F, Xu J, Jiang H, Wu H. The associations among quantitative spectral CT parameters, Ki-67 expression levels and EGFR mutation status in NSCLC. Sci Rep 2020;10:3436.

16. Chen ML, Shi AH, Li XT, Wei YY, Qi LP, Sun YS. Is there any correlation between spectral CT imaging parameters and PD-L1 expression of lung adenocarcinoma? Thorac Cancer 2020;11:362-8.

17. Moreira AL, Ocampo PSS, Xia Y, Zhong H, Russell PA, Minami Y, et al. A Grading System for Invasive Pulmonary Adenocarcinoma: A Proposal From the International Association for the Study of Lung Cancer Pathology Committee. J Thorac Oncol 2020;15:1599-610.

18. Alba AC, Agoritsas T, Walsh M, Hanna S, Iorio A, Devereaux PJ, McGinn T, Guyatt G. Discrimination and Calibration of Clinical Prediction Models: Users' Guides to the Medical Literature. JAMA 2017;318:1377-84.

19. Zhou C, Wang J, Wang B, Cheng Y, Wang Z, Han B, et al. Chinese Experts Consensus on Immune Checkpoint Inhibitors for Non-small Cell Lung Cancer (2020 Version). Zhongguo Fei Ai Za Zhi 2021;24:217-35.

20. Ricciuti B, Wang X, Alessi JV, Rizvi H, Mahadevan NR, Li YY, et al. Association of High Tumor Mutation Burden in Non-Small Cell Lung Cancers With Increased Immune Infiltration and Improved Clinical Outcomes of PD-L1 Blockade Across PD-L1 Expression Levels. JAMA Oncol 2022;8:1160-8.

21. Wang T, Fan Z, Zou L, Hou Y. Can quantitative parameters of spectral computed tomography predict lymphatic metastasis in lung cancer? a systematic review and meta-analysis. Radiother Oncol 2023;183:109643.

22. Pawelczyk K, Piotrowska A, Ciesielska U, Jablonska K, Gletzel-Plucinska N, Grzegrzolka J, Podhorska-Okolow M, Dziegiel P, Nowinska K. Role of PD-L1 Expression in Non-Small Cell Lung Cancer and Their Prognostic Significance according to Clinicopathological Factors and Diagnostic Markers. Int J Mol Sci 2019;20:824.

23. Goodsitt MM, Christodoulou EG, Larson SC. Accuracies of the synthesized monochromatic CT numbers and effective atomic numbers obtained with a rapid

kVp switching dual energy CT scanner. Med Phys 2011;38:2222-32.

24. Deniffel D, Sauter A, Fingerle A, Rummeny EJ, Makowski MR, Pfeiffer D. Improved differentiation between primary lung cancer and pulmonary metastasis by combining dual-energy CT-derived biomarkers with conventional CT attenuation. Eur Radiol 2021;31:1002-10.

25. Liu K, Wang M, Xu Y, Chen Q, Li K, Zhang L, Xie X, Shen W. Value of spectral computed tomography-derived quantitative parameters based on full volume analysis in the diagnosis of benign/malignant and pathological subtypes of solitary pulmonary nodules. Quant Imaging Med Surg 2023;13:3827-40.

26. Yu Y, Fu Y, Chen X, Zhang Y, Zhang F, Li X, Zhao X, Cheng J, Wu H. Dual-layer spectral detector CT: predicting the invasiveness of pure ground-glass adenocarcinoma. Clin Radiol 2022;77:e458-65.

27. Daoud B, Cazejust J, Tavolaro S, Durand S, Pommier R, Hamrouni A, Bornet G. Could Spectral CT Have a Potential Benefit in Coronavirus Disease (COVID-19)? AJR Am J Roentgenol 2021;216:349-54.

28. Zhang Z, Yin F, Kang S, Tuo X, Zhang X, Han D. Dual-layer spectral detector CT (SDCT) can improve the detection of mixed ground-glass lung nodules. J Cancer Res Clin Oncol 2023;149:5901-6.

29. Zhang G, Li S, Yang K, Shang L, Zhang F, Huang Z, Ren J, Zhang Z, Zhou J, Pu H, Man Q, Kong W. The value of dual-energy spectral CT in differentiating solitary pulmonary tuberculosis and solitary lung adenocarcinoma. Front Oncol 2022;12:1000028.

30. Chen M, Li X, Wei Y, Qi L, Sun YS. Spectral CT imaging parameters and Ki-67 labeling index in lung adenocarcinoma. Chin J Cancer Res 2020;32:96-104.

31. Shi W, Yang Z, Zhu M, Zou C, Li J, Liang Z, Wang M, Yu H, Yang B, Wang Y, Li C, Wang Z, Zhao W, Chen L. Correlation between PD-L1 expression and radiomic features in early-stage lung adenocarcinomas manifesting as ground-glass nodules. Front Oncol 2022;12:986579.

32. Lou X, Zhou J, Ma H, Xu S, He E, Skog S, Wang H. The Half-Life of Serum Thymidine Kinase 1 Concentration Is an Important Tool for Monitoring Surgical Response in Patients with Lung Cancer: A Meta-Analysis. Genet Test Mol Biomarkers 2017;21:471-8.

33. Jiang ZF, Wang M, Xu JL. Thymidine kinase 1 combined with CEA, CYFRA21-1 and NSE improved its diagnostic value for lung cancer. Life Sci 2018;194:1-6.

34. Lv Y, Ye J, Yin YL, Ling J, Pan XP. A comparative study for the evaluation of CT-based conventional, radiomic,

combined conventional and radiomic, and delta-radiomic features, and the prediction of the invasiveness of lung adenocarcinoma manifesting as ground-glass nodules. Clin Radiol 2022;77:e741-8.

35. Kim HJ, Cho JY, Lee YJ, Park JS, Cho YJ, Yoon HI, Chung JH, Cho S, Kim K, Lee KW, Lee JH, Lee CT. Clinical Significance of Pleural Attachment and Indentation of Subsolid Nodule Lung Cancer. Cancer Res Treat 2019;51:1540-8.